TITLE (74 characters with spaces)

Indian Ocean Salinity build-up primes Deglacial Ocean Circulation Recovery

AUTHORS

Sophie Nuber*[1,2,3], James W. B. Rae[2], Xu Zhang[4], Morten B. Andersen[1], Matthew D. Dumont[2], Huw T. Mithan[3], Yuchen Sun[5], Bas de Boer[6], Ian R. Hall[1], Stephen Barker[1]

AFFILIATIONS

[1]Cardiff University, [2]University of St. Andrews, [3]National Taiwan University, [4]Institute of Tibet Plateau Research, Chinese Academy of Science, [5]Alfred Wegener Institute, [6]Vrije Universiteit Amsterdam

ABSTRACT (162 words)

The Indian Ocean provides a source of salt for North Atlantic deep-water convection sites, via the Agulhas Leakage (AL), and may thus drive changes in the ocean's overturning circulation[6,7,8]. However, little is known about salt content variability of Indian Ocean and AL waters during past glacial cycles, and how this may influence circulation. Here we show that the glacial Indian Ocean surface salt budget was notably different from the modern, responding dynamically to changes in sea level. Indian Ocean surface salinity increases during glacial intensification peaking in glacial maxima. We find that this is due to rapid land exposure in the Indonesian archipelago induced by glacial sea level lowering, and we suggest a mechanistic link via reduced input of relatively fresh Indonesian throughflow (ITF) waters into the Indian Ocean. Using new climate model results, we show that the release of this glacial Indian Ocean salinity via the Agulhas Leakage during deglaciation can directly impact the Atlantic meridional overturning circulation and global climate.

Main (2510 words including subheadings)

The surface salinity distribution in the modern Indian Ocean differs from the distribution patterns seen in the Atlantic and Pacific Oceans at comparable latitudes (Figure 1). Tropical and subtropical Atlantic and Pacific surface waters are characterised by their enhanced warmth and salinity. This is due to their re-circulation in sunny subtropical gyres with high net-evaporation. The Indian Ocean is largely located in the tropics and sub-tropics; however, modern Indian Ocean surface conditions are notably fresher than comparable latitudes in the Atlantic and Pacific. This is due to the inflow of monsoon-derived and Pacific-origin low salinity surface and thermocline waters from the Indonesian Throughflow (ITF) (Figure 1). Inflow occurs via the Timor, Lombok, and Ombai Straits[1], as well as the Bay of Bengal[2], and is transported across the tropical Indian Ocean via the South Equatorial Current (SEC)[3,2,4]. Surface water salinity does increase within the subtropical western Indian Ocean[3], but the salt is then partially exported through an active Agulhas Leakage[5]. The addition of Indian Ocean salinity to Atlantic surface waters via the Agulhas Leakage has been proposed as a mechanism to influence global ocean circulation by enhancing the density potential at North Atlantic deep-water convection sites[6,7,8]. It is therefore possible that changes in the ITF and subsequent Indian Ocean surface salinity could impact global ocean circulation.

Here, we present coupled sea surface temperature (SST) from Mg/Ca in the planktonic foraminifer *Globigerinoides ruber* (method after ref.[9]) and oxygen isotope-and SST-based relative salinity reconstructions (method after ref.[10]) from western Indian Ocean International Ocean Discovery Program Site U1476 located in the northern entrance of the Mozambique Channel (15°49.25' S; 41°46.12' E; 2166 m) to investigate changes in the western Indian Ocean surface hydrography. This site is strongly influenced by the westward flowing SEC, with a minor contribution of recirculating waters flowing directly from the southern Indian Ocean to Madagascar, and thus tracks the hydrographic conditions of the tropical western Indian Ocean source waters that feed into the Agulhas leakage[5]. Our 1.2 million year (Ma)-long record provides the first evidence for changes in tropical western Indian Ocean hydrography beyond the Last Glacial Maximum (LGM).

Glacial salinification and warming

Our data show that western Indian Ocean surface salinity and temperature structures were significantly different from modern during Pleistocene glacial stages. ED Fig. 1 shows that western SEC temperature initially cools during glacial inception from its interglacial high. However during the middle and latter phases of glacial cycles, this cooling trend reverses and surface waters begin to warm. In the absence of other influences, this warming would be expected to cause a decrease in planktic $\delta^{18}O$[11]. However, we find planktic $\delta^{18}O$ continues to increase, suggesting an increase in $\delta^{18}O_{sw}$ and hence surface salinity. Global growth in ice volume can only account for 50% of the glacial-interglacial difference in $\delta^{18}O_{sw}$ throughout the last 1.2Ma (ED Fig. 2d). As such, our data indicate a regional increase in sea surface salinity (as well as temperature) during glacial periods. After correcting for the influence of global ice volume changes (see Methods), our ice volume-corrected $\delta^{18}O_{sw}$ ($\delta^{18}O_{sw\text{-}ivc}$) and SST data show average increases of 0.83‰ (±0.2‰ 2σ) and 4.4°C (±0.8°C 2σ), respectively across 16 glacial cycles (ED Fig. 1). Glacial salinification occurs in 15 out of 16 glacial cycles, with the onset of the glacial increase in $\delta^{18}O_{sw\text{-}ivc}$ occurring on average 20kyr prior to the glacial termination in $\delta^{18}O_{benthic}$ (Figure 2a-d, ED Fig. 1, Methods). To examine the regional consistency of this feature, we stacked SST and $\delta^{18}O_{sw\text{-}ivc}$ records across the Indian Ocean (Figures 1 and 2) by resampling each record and averaging the resulting records using a Gaussian smooth (ED Fig. 3; Methods). The resulting Indian Ocean $\delta^{18}O_{sw\text{-}ivc}$ and SST stacks show the same patterns of salinification and warming during intensification of glacial conditions (Figure 2a-d), suggesting this is an Indian Ocean-wide phenomenon. The change in water mass properties does not apply to Indian Ocean water source regions, such as the South China Sea (SCS) or the western Pacific Ocean (ED Fig. 5; Methods). It is therefore likely to be connected to dynamics in the Indian Ocean region.

Salinification not set up by atmosphere

Model simulations[12,13] and data reconstructions[14,15] show that Indian Ocean temperature and salinity may be influenced by atmospheric circulation and monsoon changes driven by precession. As such, we first examined precession-scale variability within U1476 and stacked $\delta^{18}O_{sw\text{-}ivc}$ and SST using spectral analysis. We could not find any significant precessional cycle in U1476 or in the stack, but we do identify a significant 100 kyr periodicity in both, though note that caution is necessary when interpreting the spectral analysis for the $\delta^{18}O_{sw\text{-}ivc}$ stack due to its coverage of only 345 kyr. (ED Fig. 6 and 7; Methods). This suggests that insolation-driven monsoonal variability does not drive $\delta^{18}O_{sw\text{-}ivc}$ and SST in the western Indian Ocean, and only plays a minor role for the whole tropical and subtropical Indian Ocean. The Bay of Bengal[14,15] and Arabian Sea[16,17] have been highlighted as parts of the Indian Ocean where monsoonal changes play a key role in surface ocean salinity changes which could influence the subtropical Indian Ocean. However, $\delta^{18}O_{sw\text{-}ivc}$ records from both locations also show 100 kyr periodicities within the last 1.2Ma (ED Fig. 8 and 9) suggesting a glacial cycle overprint on Bay of Bengal and Arabian Sea surface salinity. In fact, we find the same early salinification process in both the Bay of Bengal (ED Fig. 8) and Arabian Sea (ED Fig. 9 k-l) salinity reconstructions. This suggests that glacial salinification is a ubiquitous feature of the Indian Ocean, and points towards a large-scale mechanism that links changes in glacial ice volume to Indian Ocean surface hydrography. Additionally, while some climate model simulations[12,13] suggest a fresher glacial western Indian surface Ocean in line with a strengthened glacial Indian Ocean dipole compared to modern, our data indicates that the western Indian Ocean was much saltier than modern (ED Fig. 1). Hence, the mechanism for glacial Indian Ocean salinification is likely caused by ocean-intrinsic dynamics, rather than atmospheric changes.

Salinification due to sea level and ITF

We find that each Indian Ocean salinification event throughout the last 1.2Ma in the $\delta^{18}O_{sw\text{-}ivc}$ stack is induced when global mean sea level (GMSL) falls to around -48m (σ = 19m) with respect to average modern sea level (Figure 2e, f). Repeating the analysis using U1476 $\delta^{18}O_{sw\text{-}ivc}$ alone yields nearly the same GMSL threshold of -48m (σ = 17m)

(ED Fig. 2). This suggests a systematic link between glacial sea level lowering and the Indian Ocean glacial salinification process. The Indonesian archipelago is characterised as a tectonically stable collection of large shallow seas with modern depths of around 50m[18,19], and has been previously highlighted as an area of major land surface re-organisation as a result of changing sea levels[20,21]. During glacial periods, falling GMSL causes a shoaling of water depths in the Indonesian archipelago leading to the resurfacing of land if sea levels decrease further than -50m relative to today. To better characterise changes in the sea-land surface distribution as a result of GMSL variability and subsequent water depth changes, we ran a coupled Sea Level-topography model ANICE-SELEN (ref.[22]; Methods). The model provides global time-step reconstructions of land-vs-sea maps that are based on dynamical reconstructions of global ice sheet change and consideration of glacio-hydro-isostatic processes. This allows us to assess dynamic regional changes in land exposure and flooding and their relationship to GMSL. Our model results show that the greatest changes in sea-to-land surface area across the Indonesian archipelago occur when GMSL is between -2m to -8m, and -42m to -56m (ED Fig. 10). The shallower of these intervals appears to be linked to the initial exposure of shallow marine geomorphological landforms, such as shallow submarine island channels, estuaries, terraces, shore platforms, sand banks, and coral reefs. Its impact on regional circulation and Indian Ocean surface salinity is therefore small. The deeper interval is directly linked to the abrupt exposure of the Java Straits and North Australian continental shelves. The glacial resurfacing of land due to lower GMSL in the Indonesian Archipelago will have important implications for the outflow dynamics of the ITF. Indeed, we find a close correspondence between GMSL and ITF outflow strength, as reconstructed from $\delta^{13}C_{benthic}$ in the Lombok Strait[23] (Figure 2g, h). This suggests that lowering global sea levels causes a reduction in the ITF outflow due to abrupt land surfacing in the Indonesian Archipelago when GMSL falls to -48m relative to today. The Java Straits and North Australian shelves have both been previously hypothesised to influence regional circulation and surface water hydrography[20,23,24]. The exposure of North Australian shelves may reduce the outflow profile area, and therefore the outflow volume of the ITF[20,23,24], while the Java Straits influence the salinity and temperature characteristics of the ITF outflow waters that enter the Indian Ocean[23,25]. At times of high sea level stands, open Java Straits allow fresh water lenses from the South China Seas (SCS) to enter the centre of the ITF, causing a hydrographic blockage of surface waters[23]. As a result, the ITF outflow manifests itself as a predominantly thermocline outflow into the Indian Ocean. In contrast, during times of low sea level (GMSL < -48m relative to today), the closure of the Java Straits restricts the inflow of freshwater lenses, reducing the blockage and allowing a surface water driven ITF outflow[23,25]. This is important for ITF hydrography, since tropical surface waters can differ strongly from thermocline waters due to evaporation. As such, surface waters in the ITF will likely be salter and warmer than thermocline waters and will predominantly form the reduced glacial ITF[23,25]. The salinity increase we observe during glaciation in the tropical and subtropical Indian Ocean is therefore likely linked to a large glacial reduction in and slight salinification of the ITF-sourced fresh water entering the Indian Ocean.

The other important Indian Ocean gateway

In the south west, the Agulhas Leakage (AL) provides a link between the Indian and Atlantic Oceans. Changes in the AL strength can also influence surface hydrography in the Indian and Atlantic Ocean (e.g. refs.[26,27]). AL strength reconstructions suggest that its volume transport and/or surface temperature and salinity was reduced during glacials within the last 500kyr[28,29] (Figure 2i-j). This could be linked to northward shifts of the super gyre boundary or the dynamical subtropical front, coupled to changes in Southern Ocean dynamics, which diminish the outflow space for warm and salty waters between the subtropical front and the African continent[30,31]. It is possible that a weakened AL could enhance the salinification process in the Indian surface Ocean by reducing the outflow of saline waters into the Atlantic and promoting recirculation under net-evaporative conditions in the Indian Ocean. Indeed, published records suggest that the glacial reduction of the AL caused increased recirculation in the southwest Indian Ocean via the Agulhas retroflection, where high evaporation led to salinification of surface waters[26]. However, while Figure 3e and 3i-j show that the increases in $\delta^{18}O_{sw\text{-}ivc}$ were generally initiated during weak AL, in some cycles AL climbs during glacial intensification, while Indian Ocean salinity stays consistently high. Therefore, although the early glacial closure of the AL might have enhanced the initial

Indian Ocean salinification process by reducing the outflow of saline waters into the Atlantic, rising AL during glacial intensification would have countered further salinification, and so cannot be the key driving mechanism for the consistent glacial salinification we observe. Instead, we highlight a reduced ITF as the leading driver of glacial Indian Ocean salinification and note that the ITF strength proxy is consistently low during salinification intervals, supporting this idea (Figure 2g).

A salty Indian Ocean can influence AMOC

The high salinity conditions in the glacial Indian Ocean can be traced along the Agulhas current system into the AL in the compiled records (ED Fig. 3c), and thus have the potential to increase salt concentration in the south Atlantic at times when the Indian Ocean is in a salty glacial mode, and the AL is strong. Published AL reconstructions show a resumption of the AL strength at the onset of deglaciations[28,29] (Figure 2i-j), and notable peaks in salinity are seen in the AL region during deglacial Heinrich stadial events[32]. Thus, the high salinity conditions prevalent in the Indian Ocean during glacial maxima would lead to an abrupt release of highly salty waters through enhanced AL during deglaciations, especially in Heinrich stadials, with the potential of influencing downstream salt delivery to the Atlantic meridional overturning circulation (AMOC) (Figure 4). Climate model results investigating the modern AL hint towards an influence of salty Indian Ocean waters on the salinity of the Atlantic, and therefore possibly on AMOC[7]. However, little is known about the impact of a salty AL on the AMOC under glacial conditions. Our data show that the salt-potential of the AL is generally highest during glacial maxima, and would remain high during Heinrich stadial events at the onset of deglaciations, when GMSL is still < -50m relative to today, and the AL strength resumes. We therefore tested the influence of enhanced AL salt import on a suppressed AMOC during a Heinrich stadial using the fully-coupled atmosphere-ocean global circulation model COSMOS[33] (Figure 3; Methods). To simulate this, we first equilibrated the model to LGM conditions (black triangle in Figure 3d). We then performed a classic North Atlantic hosing experiment (LGM015) applying 0.15 Sv for 500 years into the so-called Ruddiman Belt (Figure 3) to generate a weakened AMOC under LGM conditions mimicking a Heinrich stadial (see ref.[33]). To test the role of an increased AL salt import to the Atlantic, the net result of enhanced deglacial leakage of particularly salty Indian Ocean water, we then conducted two freshwater extraction experiments based on LGM015 by additionally imposing constant high evaporation fluxes over the Agulhas plateau equivalent to 0.05 Sv (LGM015-SA005) and 0.1 Sv (LGM015-SA01) of freshwater extraction. This freshwater extraction occurred while freshwater hosing in the North Atlantic continued. After inducing salinification in the Agulhas plateau area, we see an AMOC recovery in both experiments occurring after ~400 years in LGM015-SA005 and ~250 years in LGM015-SA01, despite the ongoing freshwater hosing (Figure 3). This suggests that enhanced salt import via the AL can have a direct impact on a weakened AMOC and can lead to an AMOC recovery even under a persistent freshwater input in the North Atlantic, which might be expected during deglaciation[8]. Our results further suggest that the elevated amount of salt imported into the South Atlantic has an effect on the response time of the AMOC, with higher salinities leading to faster response times. This underlines that the glacial salinification process in the tropical and subtropical Indian surface Ocean can play an important role for not only the global overturning circulation, but also the shape of deglaciations, depending on the amount of salt harvested throughout the glacial, and the speed of release through the AL. In summary, we highlight the dynamic interplay between different components of the climate system during glacial cycles, showing that falling sea levels during glacial intensification restrict ITF, in turn salinifying the Indian Ocean, which may ultimately trigger abrupt changes in AMOC and shape glacial termination.

MAIN TEXT REFERENCES

1. Sprintall, J., Wijffels, S. E., Molcard, R., & Jaya, I. (2009). Direct estimates of the indonesian throughflow entering the indian ocean: 2004-2006. *Journal of Geophysical Research: Oceans*, *114*(7). https://doi.org/10.1029/2008JC005257
2. Sengupta, D., Bharath Raj, G. N., & Shenoi, S. S. C. (2006). Surface freshwater from Bay of Bengal runoff and Indonesian Throughflow in the tropical Indian

Ocean. *Geophysical Research Letters*, *33*(22). https://doi.org/10.1029/2006GL027573

3. Talley, L. D., & Sprintall, J. (2005). Deep expression of the Indonesian Throughflow: Indonesian Intermediate Water in the South Equatorial Current. *Journal of Geophysical Research*, *110*(C10), C10009. https://doi.org/10.1029/2004JC002826
4. Gordon, A. L., Ma, S., Olson, D. B., Hacker, P., Ffield, A., Talley, L. D., Wilson, D., & Baringer, M. (1997). Advection and diffusion of Indonesian Throughflow Water within the Indian Ocean South Equatorial Current. *Geophysical Research Letters*, *24*(21), 2573–2576. https://doi.org/10.1029/97GL01061@10.1002/(ISSN)1944-8007.WOCEEX1
5. Durgadoo, J. V., Rühs, S., Biastoch, A., & Böning, C. W. B. (2017). Indian Ocean sources of Agulhas leakage. *Journal of Geophysical Research: Oceans*, *122*(4), 3481–3499. https://doi.org/10.1002/2016JC012676
6. Beal, L. M., De Ruijter, W. P. M., Biastoch, A., Zahn, R., Cronin, M., Hermes, J., Lutjeharms, J., Quartly, G., Tozuka, T., Baker-Yeboah, S., Bornman, T., Cipollini, P., Dijkstra, H., Hall, I., Park, W., Peeters, F., Penven, P., Ridderinkhof, H., & Zinke, J. (2011). On the role of the Agulhas system in ocean circulation and climate. In *Nature* (Vol. 472, Issue 7344, pp. 429–436). https://doi.org/10.1038/nature09983
7. Biastoch, A., Böning, C. W., Schwarzkopf, F. U., & Lutjeharms, J. R. E. (2009). Increase in Agulhas leakage due to poleward shift of Southern Hemisphere westerlies. *Nature*, *462*(7272), 495–498. https://doi.org/10.1038/nature08519
8. Knorr, G., & Lohmann, G. (2003). Southern ocean origin for the resumption of Atlantic thermohaline circulation during deglaciation. *Nature*. https://doi.org/10.1038/nature01855
9. Gray, W. R., & Evans, D. (2019). Nonthermal Influences on Mg/Ca in Planktonic Foraminifera: A Review of Culture Studies and Application to the Last Glacial Maximum. *Paleoceanography and Paleoclimatology*, *34*(3), 306–315. https://doi.org/10.1029/2018PA003517

10. Kiefer, T., McCave, I. N., & Elderfield, H. (2006). Antarctic control on tropical Indian Ocean sea surface temperature and hydrography. *Geophysical Research Letters*, *33*(24), L24612. https://doi.org/10.1029/2006GL027097
11. Waelbroeck, C., Mulitza, S., Spero, H., Dokken, T., Kiefer, T., & Cortijo, E. (2005). A global compilation of late Holocene planktonic foraminiferal δ18O: relationship between surface water temperature and δ18O. *Quaternary Science Reviews*, *24*(7–9), 853–868. https://doi.org/10.1016/J.QUASCIREV.2003.10.014
12. DiNezio, P. N., Tierney, J. E., Otto-Bliesner, B. L., Timmermann, A., Bhattacharya, T., Rosenbloom, N., & Brady, E. (2018). Glacial changes in tropical climate amplified by the Indian Ocean. *Science Advances*, *4*(12). https://doi.org/10.1126/sciadv.aat9658
13. Thirumalai, K., DiNezio, P. N., Tierney, J. E., Puy, M., & Mohtadi, M. (2019). An El Niño Mode in the Glacial Indian Ocean? *Paleoceanography and Paleoclimatology*, *34*(8), 1316–1327. https://doi.org/10.1029/2019PA003669
14. Clemens, S. C., Yamamoto, M., Thirumalai, K., Giosan, L., Richey, J. N., Nilsson-Kerr, K., Rosenthal, Y., Anand, P., & McGrath, S. M. (2021). Remote and local drivers of Pleistocene South Asian summer monsoon precipitation: A test for future predictions. *Science Advances*, *7*(23), eabg3848. https://doi.org/10.1126/sciadv.abg3848
15. Nilsson-Kerr, K., Anand, P., Sexton, P. F., Leng, M. J., & Naidu, P. D. (2022). Indian Summer Monsoon variability 140–70 thousand years ago based on multi-proxy records from the Bay of Bengal. *Quaternary Science Reviews*, *279*, 107403. https://doi.org/10.1016/J.QUASCIREV.2022.107403
16. Ishikawa, S., & Oda, M. (2007). Reconstruction of Indian monsoon variability over the past 230,000 years: Planktic foraminiferal evidence from the NW Arabian Sea open-ocean upwelling area. *Marine Micropaleontology*, *63*(3–4), 143–154. https://doi.org/10.1016/J.MARMICRO.2006.11.004
17. Kumar K., P., & Ramesh, R. (2017). Revisiting reconstructed Indian monsoon rainfall variations during the last ∼25 ka from planktonic foraminiferal δ18O from the Eastern Arabian Sea. *Quaternary International*, *443*, 29–38. https://doi.org/10.1016/J.QUAINT.2016.07.012

18. Hanebuth, T. J. J., & Stattegger, K. (2004). Depositional sequences on a late Pleistocene–Holocene tropical siliciclastic shelf (Sunda Shelf, southeast Asia). *Journal of Asian Earth Sciences*, *23*(1), 113–126. https://doi.org/https://doi.org/10.1016/S1367-9120(03)00100-7
19. Kudrass, H. R., & Schlüter, H. U. (1994). Development of cassiterite-bearing sediments and their relation to late Pleistocene sea-level changes in the Straits of Malacca. *Marine Geology*, *120*(3), 175–202. https://doi.org/https://doi.org/10.1016/0025-3227(94)90058-2
20. Petrick, B., Martínez-García, A., Auer, G., Reuning, L., Auderset, A., Deik, H., Takayanagi, H., De Vleeschouwer, D., Iryu, Y., & Haug, G. H. (2019). Glacial Indonesian Throughflow weakening across the Mid-Pleistocene Climatic Transition. *Scientific Reports*, *9*(1). https://doi.org/10.1038/s41598-019-53382-0
21. Hanebuth, T. J. J., Voris, H. K., Yokoyama, Y., Saito, Y., & Okuno, J. (2011). Formation and fate of sedimentary depocentres on Southeast Asia's Sunda Shelf over the past sea-level cycle and biogeographic implications. *Earth-Science Reviews*, *104*(1), 92–110. https://doi.org/https://doi.org/10.1016/j.earscirev.2010.09.006
22. de Boer, B., Stocchi, P., & van de Wal, R. S. W. (2014). A fully coupled 3-D ice-sheet–sea-level model: algorithm and applications. *Geoscientific Model Development*, *7*(5), 2141–2156. https://doi.org/10.5194/gmd-7-2141-2014
23. Holbourn, A., Kuhnt, W., & Xu, J. (2011). Indonesian Throughflow variability during the last 140 ka: The timor sea outflow. *Geological Society Special Publication*, *355*, 283–303. https://doi.org/10.1144/SP355.14
24. Gordon, A. L., Susanto, R. D., & Vranes, K. (2003). Cool Indonesian throughflow as a consequence of restricted surface layer flow. *Nature*, *425*(6960), 824–828. https://doi.org/10.1038/nature02038
25. Sarr, A. C., Husson, L., Sepulchre, P., Pastier, A. M., Pedoja, K., Elliot, M., Arias-Ruiz, C., Solihuddin, T., Aribowo, S., & Susilohadi. (2019). Subsiding sundaland. *Geology*, *47*(2), 119–122. https://doi.org/10.1130/G45629.1

26. Simon, M. H., Arthur, K. L., Hall, I. R., Peeters, F. J. C., Loveday, B. R., Barker, S., Ziegler, M., & Zahn, R. (2013). Millennial-scale Agulhas Current variability and its implications for salt-leakage through the Indian-Atlantic Ocean Gateway. *Earth and Planetary Science Letters*, *383*, 101–112. https://doi.org/10.1016/j.epsl.2013.09.035

27. Dickson, A. J., Leng, M. J., Maslin, M. A., Sloane, H. J., Green, J., Bendle, J. A., Mcclymont, E. L., Pancost, R. D., Dickson, C. :, Leng, M. J., Maslin, M. A., Sloane, H. J., Green, J., Bendle, J. A., Mcclymont, E. L., & Pancost, R. D. (2010). Atlantic overturning circulation and Agulhas leakage influences on southeast Atlantic upper ocean hydrography during marine isotope stage 11. *Paleoceanography*, *25*(3). https://doi.org/10.1029/2009PA001830

28. Peeters, F. J. C., Acheson, R., Brummer, G. J. A., De Ruijter, W. P. M., Schneider, R. R., Ganssen, G. M., Ufkes, E., & Kroon, D. (2004). Vigorous exchange between the Indian and Atlantic oceans at the end of the past five glacial periods. *Nature*, *430*(7000), 661–665. https://doi.org/10.1038/nature02785

29. Caley, T., Giraudeau, J., Malaizé, B., Rossignol, L., & Pierre, C. (2012). Agulhas leakage as a key process in the modes of Quaternary climate changes. *Proceedings of the National Academy of Sciences of the United States of America*, *109*(18), 6835–6839. https://doi.org/10.1073/pnas.1115545109

30. Bard, E., & Rickaby, R. E. M. (2009). Migration of the subtropical front as a modulator of glacial climate. *Nature*, *460*(7253), 380–383. https://doi.org/10.1038/nature08189

31. De Boer, A. M., Graham, R. M., Thomas, M. D., and Kohfeld, K. E. (2013). The control of the Southern Hemisphere Westerlies on the position of the Subtropical Front. J. Geophys. Res. Oceans, 118, 5669– 5675, https://doi.org/10.1002/jgrc.20407

32. Marino, G., Zahn, R., Ziegler, M., Purcell, C., Knorr, G., Hall, I. R., Ziveri, P., & Elderfield, H. (2013). Agulhas salt-leakage oscillations during abrupt climate changes of the Late Pleistocene. *Paleoceanography*, *28*(3), 599–606. https://doi.org/10.1002/palo.20038

33. Zhang, X., Lohmann, G., Knorr, G., & Xu, X. (2013). Different ocean states and transient characteristics in Last Glacial Maximum simulations and implications for deglaciation. *Climate of the Past*, *9*(5), 2319–2333. https://doi.org/10.5194/cp-9-2319-2013

FIGURE LEGENDS

Fig. 1 Geographic and hydrographic context of study sites

Modern ocean surface salinity distribution[34] and GEBCO2014 bathymetry[35] plotted using Ocean Data view[36], and orange-to-blue salinity scale, where white represents mean ocean water ~35 psu, with key surface circulation patterns and study sites. Fresher and saltier water mass pathways are indicated with blue and orange arrows, respectively. Location numbers as follows: pink star ④ U1476 (this study); pink circles ① ODP1087[29, 37], ② Agulhas Bank Splice (ABS)[38], ③ MD96-2048[39], ④ U1476 (this study), ⑤ WIND28K[10], ⑥ TY93-929/P[40], ⑦ MD90-0963[41,42], ⑧ GeoB10038-4[43], ⑨ MD01-2378[44,45], ⑩ ODP1146[46], ⑪ ODP806[47]. Sites ② – ⑨ are used in our Indian Ocean data stacks. Abbreviations include Agulhas counter current (CC), South China Sea (SCS), Indonesian throughflow (ITF), and west Pacific warm pool (WPWP).

Fig. 2 Records of Indian Ocean surface salinification and warming compared to changes in Indonesian throughflow and sea level

(a) Sea surface temperature (SST) stack (z-scores relative to mean and $\sigma = 1$) for the Indian Ocean (bold orange line, from 0 - 790 ka) with upper and lower 95th percentile indicated by orange shaded envelope, and prior to 790 ka, SST data exclusively from U1476 SST (thin orange line; this study). (b), (d) LR04 benthic $\delta^{18}O$[48] with inverted y-axes (grey line). (c), (e) Ice volume-corrected $\delta^{18}O_{sw}$ stack (z-scores) for the Indian surface Ocean (bold green line from 0 – 345 ka) with upper and lower 95th percentile indicated by green shaded envelope, and prior to 345 ka, ice volume-corrected $\delta^{18}O_{sw}$ data exclusively from U1476 (thin green line; this study). Green diamonds in (e) indicate the onset of glacial $\delta^{18}O_{sw\text{-}ivc}$ increase within each glacial cycle. (f), (h) global mean sea level[49] (GMSL, pink line), in (f) with GMSL at onset of $\delta^{18}O_{sw\text{-}ivc}$ increases (green diamonds in (e)), horizontal dashed pink line is the average value of all pink circles. (g) Detrended Indonesian throughflow (ITF) outflow strength proxy[23] (blue line). (i) Agulhas Leakage proxy using Agulhas Leakage Fauna (ALF) counts[28] (light grey area). (j) Agulhas Leakage proxy using *G. menardii* counts[29] (dark grey spikes). Intervals of rising $\delta^{18}O_{sw\text{-}ivc}$ -stack prior to each glacial termination are indicated with vertical grey bars. Glacial terminations are labelled at the top, and indicated with dashed vertical lines.

Fig. 3 Role of intrusion of salinification Indian water mass in deglacial AMOC strength

(a) Sea surface salinity anomaly between the normal LGM background experiment (LGM) which is equivalent to the LGM-W experiment in ref.[33], and the Heinrich-stadial experiment including North Atlantic freshwater hosing (LGM015). (b) and (c) sea surface salinity anomaly between the Heinrich-stadial background setting (experiment LGM015) and anomalies of saltwater hosing experiments equivalent to removal of 0.1 Sv freshwater (LGM015-SA01), and 0.05 Sv freshwater (LGM015-SA005). The average in (b), and (c) respectively, was calculated from the 160th to 210th, and 290th to 340th, model year window. Green and purple rectangles in (a) indicate freshwater hosing and freshwater extraction ("saltwater hosing") in the North and South Atlantic. (d) and (e) time series of AMOC indices and Agulhas Leakage salinity (average in 5° E ~ 20° E and 30° S ~ 40° S). AMOC index from the LGM background climate run (no freshwater hosing), indicated with a black arrow marker (~18 Sv). The AMOC index is defined as the maximum value of the stream function below the water depth of 500 m north of 45° N in the North Atlantic. The map was plotted using the numerical computing environment and programming language Matlab developed by MathWorks. PMIP3 LGM topography/bathymetry were taken from ref[33] according to the PMIP protocol[50].

Fig. 4 Proposed links between sea-level induced changes in the Indonesian throughflow, Indian surface ocean salinity, and efficiency of Agulhas leakage

(a) During interglacials and glaciation, when sea level (SL) is higher than -50 m relative to today, the Indonesian archipelago is submerged leading to a strong Indonesian throughflow (ITF) and import of fresher waters into the Indian Ocean (IO) along the South Equatorial Current (SEC). This coincides with a moderately efficient Agulhas Leakage (AL) south of Africa where the subtropical front (SF) is located further south. (b) During the latter half of the glacial cycle, Indonesian archipelago channels and shallow seas are exposed due to SL lower than -50m relative to today, reducing the ITF and minimising the import of fresher waters into the IO. This coincides with equatorward-shifted glacial SF conditions and a reduced glacial AL. (c) During the onset of deglaciations, the ITF is still reduced because the Indonesian archipelago is still exposed (SL lower than -50m relative to today). However, poleward shift of the SF causes a resumption of the AL which releases highly salty Indian Ocean waters into the South Atlantic. Note all colour bars and patterns are for descriptive purposes only. Top and side panels were plotted using Ocean Data view[36] and bathymetry[35], respectively.

METHODS (2754 words including subheadings)

Age model

The age model for U1476 was taken from ref.[51] who aligned U1476 $\delta^{18}O_{benthic}$ to the $\delta^{18}O_{benthic}$ probability stack[52].

SST and relative salinity derivation

Globigerinoides ruber (*G. ruber*) samples were picked from U1476, then crushed and homogenised. An aliquot of 5 foraminifera was analysed for $\delta^{18}O$ on a MAT253 with a Kiel IV preparation device at Cardiff University. The remaining samples were cleaned and dissolved in a fume hood equipped with HEPA filters under clean laboratory conditions according to ref.[39]. Analysis of Mg/Ca was conducted partially on a Thermo Element XR at Cardiff University, partially on an Agilent Triple Quadrupole at the University of St. Andrews. The instruments were cross-calibrated using the same in-house standard. In both institutions, long term reproducibility of in-house standards yielded RSDs of 1-3 %.

SST were calculated from *G. ruber* Mg/Ca using the transfer function and R-script from ref.[9]

$$\frac{Mg}{Ca} = e^{0.060(\pm 0.008)xT + 0.033(\pm 0.022)xS - 0.83(\pm 0.73)x(pH-8) - 1.07(\pm 0.80)}$$

where T is sea surface temperature, S is salinity, and pH is the negative decadic logarithm of H^+ ions. The method[9] allows for the influence of pH and salinity on Mg/Ca, and calculates SST and pH iteratively using Mg/Ca and Antarctic ice core pCO_2[53]. This underlies the assumption that the core site has been at CO_2 equilibrium, or constant disequilibrium throughout the record[9]. Global ocean salinity and alkalinity are calculated from the LR04 benthic $\delta^{18}O$ stack[48] at each time step with modern salinity assumed as 35 psu and modern alkalinity at 2300 µmol/kg[9]. For Late Pleistocene records, pCO_2 can be taken from ice core measurements[53]. Our data exceeds the maximum length of the ice core by several thousand years. We therefore scale the LR04 benthic $\delta^{18}O$ stack[48] to the ice core pCO_2 record[53] (see ED Fig. 2a, b) to provide an estimate of CO_2 change and assign a conservative uncertainty of ±40 µatm (2 σ)[9]. SST uncertainties are calculated using Monte-Carlo propagation analysis which accounts for errors on Mg/Ca measurement, SST-equation-calibration errors, salinity errors prescribed as ±1 psu (2 σ), LR04 age model errors prescribed as 4 kyr, alkalinity uncertainty prescribed as -25 to +75 µmol/kg about the modern value using a flat probability distribution[9].

Ice volume-corrected seawater $\delta^{18}O$ ($\delta^{18}O_{sw\text{-}ivc}$) has been previously used as a proxy for changes in relative seawater salinity in the surface Indian Ocean (e.g. ref.[10]). We therefore correct our $\delta^{18}O_{carbonate}$ according to

$$\delta^{18}O_{sw\text{-}ivc} = \delta^{18}O_{carbonate} - \delta^{18}O_{temperature} - \delta^{18}O_{ice\ volume}$$

to reflect local $\delta^{18}O_{sw}$ and interpret the results as changes in relative salinity. $\delta^{18}O_{temperature}$ was calculated from Mg/Ca-based temperatures and $\delta^{18}O_{\textit{G. ruber}}$ using the transfer function of ref.[54] for Indian Ocean planktonic foraminifera with a correction factor of +0.20[55]. Analytical errors from $\delta^{18}O_{carbonate}$ and Monte-Carlo-errors from SST were propagated through the calculation. To determine the best correction curve for $\delta^{18}O_{ice\ volume}$ across the last 1.2Ma, we tested the impact of 4 different sea level reconstructions on the resulting $\delta^{18}O_{sw\text{-}ivc}$ (ED Fig. 4). Reconstructions of $\delta^{18}O_{ice\ volume}$ from ref.[49] based on the LR04 stack[48] gave representative results over the last ~500 kyr where different sea level reconstructions can be readily compared and also extends for the ~1.2 Myr duration of our record, and was therefore used to determine $\delta^{18}O_{sw\text{-}ivc}$. In Figures 2 and ED Fig. 2, we compare the U1476 $\delta^{18}O_{sw\text{-}ivc}$ record to GMSL and the change in land/sea area in the Indonesian archipelago both of which are based on calculations using the U1476 $\delta^{18}O_{benthic}$ record[51]. Using $\delta^{18}O_{ivc}$ from ref.[49] as a correction factor may lead to age model uncertainties when comparing U1476 $\delta^{18}O_{sw\text{-}ivc}$ to U1476 $\delta^{18}O_{benthic}$[51], and -related results. We therefore also corrected the U1476 $\delta^{18}O_{sw\text{-}ivc}$ record with $\delta^{18}O_{ivc}$ modelled in ANICE using U1476 $\delta^{18}O_{benthic}$[51]. The resulting age model differences are minimal. For example, when correcting U1476 $\delta^{18}O_{sw}$ with U1476 $\delta^{18}O_{ivc}$, salinification occurs at GMSL of -45 m (σ = 17 m) relative to today which is nearly the same as calculated for the $\delta^{18}O_{sw\text{-}ivc}$ stack and U1476 $\delta^{18}O_{sw\text{-}ivc}$ corrected using $\delta^{18}O_{ivc}$ from ref.[51].

To analyse the lead-lag time between our $\delta^{18}O_{sw\text{-}ivc}$, and SST data with $\delta^{18}O_{benthic}$[51], we performed a cross spectral analysis **using the ARAND software package (new ref)** between $\delta^{18}O_{sw\text{-}ivc}$, or SST, and $\delta^{18}O_{benthic}$[51] . Both records were first clipped to 1350 ka, then subsampled to 1 kyr. The resulting cross spectral analysis calculated an average lead time of 18 kyr in the $\delta^{18}O_{sw\text{-}ivc}$, and 14 kyr in SST to $\delta^{18}O_{benthic}$ at the 95 % confidence interval in the 100-ka periodicity. The phasing results show that both $\delta^{18}O_{sw\text{-}ivc}$ and SST lead $\delta^{18}O_{benthic}$ at the 95 % confidence interval.

SST and $\delta^{18}O_{sw\text{-}ivc}$ stack formation

The data for the SST and $\delta^{18}O_{sw\text{-}ivc}$ stacks was taken from 8 cores spread across the Indian Ocean. We included all cores covering at least the Holocene and LGM at 3 - 4 kyr resolution which represent open ocean environments (i.e. to avoid coastal influences), and were able to provide: Mg/Ca- or alkenone-based SST data for the SST stack; Mg/Ca-based SST, and surface foraminifera-based $\delta^{18}O$ for the $\delta^{18}O_{sw\text{-}ivc}$ stack. The resulting stacks include the following cores: Agulhas Bank Slice (ABS) (Mg/Ca$_{\mathit{G.\ bulloides}}$, $\delta^{18}O_{\mathit{G.\ bulloides}}$)[38], MD96-2048 (SST$_{Alkenone}$, $\delta^{18}O_{\mathit{C.\ wuellerstorfi}}$)[39], U1476 (Mg/Ca$_{\mathit{G.\ ruber}}$

and $\delta^{18}O_{G.ruber}$, this study; $\delta^{18}O_{C.\ wuellerstorfi}$[51]), WIND 28K (Mg/$Ca_{G.\ ruber}$, $\delta^{18}O_{G.\ ruber}$, $\delta^{18}O_{C.\ wuellerstorfi}$)[10], TY93-929/P (Mg/$Ca_{G.\ ruber}$, $\delta^{18}O_{G.\ ruber}$)[40], MD90-0963 ($SST_{Alkenone}$, $\delta^{18}O_{G.\ ruber}$)[41,42], GeoB10038-4 (Mg/$Ca_{G.\ ruber}$, $\delta^{18}O_{G.\ ruber}$, $\delta^{18}O_{C.\ wuellerstorfi}$)[43], and MD01-2378 (Mg/$Ca_{G.\ ruber}$, $\delta^{18}O_{G.\ ruber}$)[44,45]. We first re-calculated SST and $\delta^{18}O_{sw\text{-}ivc}$ data from all cores using the same method as described in the methods above for U1476 to ensure methodological consistency. The SST and $\delta^{18}O_{sw\text{-}ivc}$ stacks were then created by splicing the records together and resampling by replacement within a moving 15 kyr window centred on each real data point. The probability of selecting each data point within the window was adjusted using two weights. The first uses a gaussian function (σ = 3 kyr) to weight each point based on its distance from the centre of the window, thus favouring closer data. The second weight is inversely proportional to the relative representation of a given component record within the sampling window, thus acting to mitigate sampling bias. The resampling was performed throughout the spliced record 1000 times to produce a smoothed stack with 95% confidence intervals. Figure 2 in the main manuscript shows z-scores of the stacks.

We also incorporate age model uncertainties into the stack uncertainty. Because each of the component records used in the stack use a combination of radiocarbon and $\delta^{18}O$ alignment, we take a simple conservative approach and apply a 4 kyr uncertainty[48] to the age models based on the estimated uncertainty for $\delta^{18}O$ alignment. This uncertainty was incorporated into the stack by adapting the method of ref.[56], which involves applying an age shift of -2, -1, 0, +1, or +2 kyr (chosen with equal probability) independently to each record during the construction of each of the 1000 synthetic records. $\delta^{18}O$ data are shown from each core alongside LR04[48] in ED Fig. 3a and demonstrate a close alignment of age models for these cores on glacial-interglacial timescales.

Alternative hypothesis testing

To test whether the salinification process is also evident in Indian Ocean source waters, we additionally analysed SST core data from the western Pacific warm pool (ODP806)[47] and the South China Sea (ODP1146)[46] for lead-lag against their respective

$\delta^{18}O_{benthic}$ using cross spectral analysis. For the analysis, SST and $\delta^{18}O_{benthic}$ data from the cores was clipped to 6 - 1168 ka, then subsampled at 1 kyr. The cross spectral analysis was conducted between the SST data and their respective $\delta^{18}O_{benthic}$ from the same core using the resampled data. Neither core ODP806[47] or ODP1146[46] showed a significant SST lead at the 95 % confidence interval.

We also used spectral analysis to test whether insolation or monsoon dynamics drive our records. For this purpose, we used U1476, our calculated Indian Ocean surface $\delta^{18}O_{sw-ivc}$ stack, and ocean sediment core U1446 from the Bay of Bengal[14]. We find no significant peak in the precession band for U1476 $\delta^{18}O_{sw-ivc}$ and the Indian Ocean $\delta^{18}O_{sw-ivc}$ stack (ED Fig. 8), and no visual correlation between U1476 $\delta^{18}O_{sw-ivc}$ and 15° S July insolation[57] or African[58], Indian[59] or Southeast Asian[60] monsoonal proxies (ED Fig. 9 c-j). As already pointed out by the authors, there is a significant precession peak for U1446[14] (ED Fig. 8). However, the most significant peak occurs in the 100 kyr periodicity in all records (ED. Figs. 6 - 8). We therefore conclude that insolation and monsoonal changes do not influence U1476 and that the monsoon signal in Indian Ocean salinity records is overprinted by an ice volume signal to different degrees.

ANICE-SELEN sea level-topography model

Simulations of local relative sea level around the Indonesian archipelago were executed using the coupled ice sheet – topography model ANICE-SELEN[22,61]. The 3D ice-sheet model ANICE produces a paleo-GMSL record and, in this study, is forced with U1476 $\delta^{18}O_{benthic}$ data, which acts as a proxy for global ice sheet volume[62,63] while also minimising age model uncertainty in comparisons of model output to our data. Additional inputs of present-day meteorological information, basal and ice sheet height topography for Greenland and Antarctica, and higher resolution topography for currently ice-free Eurasia and North America[61] allow it to solve the ice sheet mass balance for four global ice sheets Greenland, Antarctica, Eurasia, and North America on a 2D grid[61]. This is achieved by decomposing the $\delta^{18}O_{benthic}$ record into its ice volume and deep-water temperature components using an inverse approach, modelling from the past into the present day[61], where information from the $\delta^{18}O_{benthic}$

data determines the mass balance, and in return mass balance results influence the modelled $\delta^{18}O$. The approach assumes that changes in Northern hemisphere (NH) mid latitude-to-subpolar surface-air temperature anomalies (ΔT_{NH}) are strongly related to changes in ice volume and deep-water formation. Changes in ΔT_{NH} are derived from the difference between modelled $\delta^{18}O$ at time t, and foraminiferal $\delta^{18}O_{benthic}$ at time t + 100 years[61]. Bedrock deformations due to changes in ice volume and resulting influences on GMSL are considered by allowing a downward deflection of the flat elastic lithosphere into a viscous asthenosphere as a result of pressure exerted from above. The SELEN model solves the sea level equation (SLE) accounting for glacial-hydro-isostatic adjustment on a global mesh[22]. In the coupled ANICE-SELEN version, ANICE's ice sheet thickness information, in addition to initial topography information which we assume to be present-day topography in this study, is used to calculate local sea level stands at each GMSL time step as a result of glacial-hydro-isostatic adjustment [22]. Any time lags in isostatic adjustment are accounted for by predicting the effect of sea level change within the next 15 time-steps (around 15 000 years). This information is also returned to ANICE, leading to a more accurate prediction of ice sheet height in the four regional ice sheet models. During times of transient ice sheet height changes, the predicted effect is continuously updated and considers the influence of previous multiple time-steps on the time-step currently calculated[22]. In the end, ANICE-SELEN exports two important variables which involve (i) a reconstruction of GMSL as time transient curve, and (ii) a reconstruction of the local sea level changes as geospatial maps which are made up of land and ocean pixels.

To gain understanding of the land surfacing and flooding rates around the Indonesian archipelago across the Middle to Late Pleistocene (ED Fig. 10), we began running ANICE from t = 1.4 Ma, then started the coupling process at 1.35 Ma with a 100 kyr spin-up period (about 3 glacial cycles) to equilibrate the time-lag in isostatic adjustment. To increase model-run efficiency, we disconnected SELEN after 10 glacial cycles at 0.65 Ma, and ended ANICE modelling at t =0 Ma. We extracted 598 global topography maps from the period between 1250 ka and 651 ka at a temporal resolution of 1 kyr and a spatial resolution of 1 pixel per ~5000 km^2. Each topography map is linked to a period of time, where a GMSL value is calculated from ANICE. Since the tectonics and geomorphology of the Indonesian Archipelago appear relatively constant across the last 1.2 Ma[18,19], we assume that any correlations between changes in the land-ocean ratio and GMSL should also be valid for younger glacial cycles. To calculate changes in above-sea level topography, all maps were processed in Python and cut to the same size, zooming in on the Indonesian archipelago (ED Fig. 10a). Each pixel was given a value of 0, or 1, for ocean, or land, respectively. Then, all pixels of the same value were counted up, and land-to-ocean ratios were calculated for each map as

$$R_{land-ocean} = \frac{\sum Pixel_{land}}{\sum Pixel_{ocean}}$$

Changes in the land-to-ocean ratio with respect to GMSL [m] were calculated as

$$\Delta R_{land-ocean} = \frac{R_{land-ocean}\big(GMSL(t+1)\big) - R_{land-ocean}(GMSL(t))}{GMSL(t+1) - GMSL(t)}$$

To identify trends in the sea/land ratio linked to regionally rising and falling sea level, we analysed peaks and troughs in the global mean sea level curve and defined the time between a peak and a trough as “falling”, and between a trough and a peak as “rising”. The land-ocean ratios corresponding to the different time slices were then sorted into ratios during rising, and ratios during falling GMSL, to understand the dynamics of sea/land changes that occur during rising GMSL and falling GMSL, respectively (see ED Fig. 10).

Salinity influence on AMOC in COSMOS

Four ocean circulation experiments were conducted in the comprehensive climate model COSMOS[33]. These include the LGM (no freshwater hosing) control experiment, the LGM015 (freshwater hosing into the North Atlantic) experiment, the LGM015-SA01 (freshwater extraction in the South Atlantic equivalent to “saltwater hosing” in addition to freshwater hosing in the North Atlantic) experiment, and the LGM015-SA005 (weaker freshwater extraction in the South Atlantic equivalent to “saltwater hosing” in addition to freshwater hosing in the North Atlantic) experiment. Glacial state control settings are taken from the LGM-W experiment from ref.[33] which currently provide the closest match with proxy data We allowed the model to run until the glacial control settings were equilibrated (LGM experiment). Since deglaciations begin with Heinrich events during which the AMOC is strongly suppressed, we perturbed the equilibrium state glacial ocean circulation by imposing a constant 0.15 Sv freshwater perturbation over the ice-rafted debris belt in the North Atlantic for 500 years (LGM015) (Figure 3) representative of a 10 m/kyr GMSL rise (see also ref.[33]). We then investigated effects of additional salinity perturbations on the Agulhas plateau by removing freshwater from the region through enhanced evaporation. Two salt-water perturbation experiments with evaporation equivalent of the removal of 0.05Sv (LGM015-SA005) and 0.1 Sv (LGM015-SA01) freshwater, representing 1/3 and 2/3 of the freshwater hosing force, were integrated for 800 years based on LGM015 (i.e. under the background climate of persistent freshwater input in the North Atlantic) (Figure 3). In addition, LGM015 is continued for additional 800 years to provide a control run for AMOC changes in LGM015-SA005 and LGM015-SA01. We plot AMOC variability as the AMOC index in Figure 3. Here, we define the AMOC index as the maximum value of the stream function below the water depth of 500m north of 45° N in the North Atlantic in depth-space, effectively representing changes in the rate of North Atlantic deep-water formation and AMOC.

DATA AVAILABILITY

The geochemical datasets produced in this study are freely available at the data repository Pangea.

CODE AVAILABILITY

Python code was used to calculate the stacks, and analyse the ANICE-SELEN image outputs. Both are freely available on Zenodo, for stack calculation (https://zenodo.org/record/7478552; DOI: 10.5281/zenodo.7478552), and ANICE-SELEN image processing (https://zenodo.org/record/7471500; DOI 10.5281/zenodo.7471500).

ADDITIONAL REFERENCES

34. Lauvset, S. K., Lange, N., Tanhua, T., Bittig, H. C., Olsen, A. C., Kozyr, A., Àlvarez, M., Becker, S., Brown, P. J., Carter, B. R., Cotrim da Cunha, L., Feely, R. A., van Heuven, S., Hoppema, M., Ishii, M., Jeansson, E., Jutterström, S., Jones, S. D., Karlsen, M. K., Lo Monaco, C., Michaelis, P., Murata, A., Pérez, F. F., Pfeil, B., Schirnick, C., Steinfeldt, R., Suzuki, T., Tilbrook, B., Velo, A., Wanninkhof, R., Woosley, R. J., and Key, R. M. (2021). An updated version of the global interior ocean biogeochemical data product, GLODAPv2.2021. *Earth System Sciences Data Discussion, 1-32.* https://doi.org/10.5194/essd-2021-234
35. Weatherall, P., Marks, K. M., Jakobsson, M., Schmitt, T., Tani, S., Arndt, J. E., Rovere, M., Chayes, D., Ferrini, V., & Wigley, R. (2015). A new digital bathymetric model of the world's oceans. *Earth and Space Science*, *2*(8), 331–345. https://doi.org/10.1002/2015EA000107
36. Schlitzer, Reiner, Ocean Data View, https://odv.awi.de, 2021
37. Pierre, C., Saliège, J. F., Urrutiaguer, M. J., & Giraudeau, J. (2001). *Stable isotope record of benthic and planktonic foraminifera from ODP Site 175-1087 in the southern Cape Basin, Atlantic Ocean*. PANGAEA. https://doi.org/10.1594/PANGAEA.701338
38. Martinez-Mendez, G., Zahn, R., Hall, I. R., Peeters, F. J. C., Pena, L. D., Cacho, I., & Negre, C. (2010). Contrasting multiproxy reconstructions of surface ocean hydrography in the Agulhas Corridor and implications for the Agulhas Leakage during the last 345,000 years. *Paleoceanography*, *25*(4). https://doi.org/10.1029/2009PA001879
39. Caley, T., Kim, J.-H., Malaizé, B., Giraudeau, J., Laepple, T., Caillon, N., Charlier, K., Rebaubier, H., Rossignol, L., Castañeda, I. S., Schouten, S., & Sinninghe Damsté, J. S. (2011). High-latitude obliquity as a dominant forcing in the Agulhas current system. *Climate of the Past*, *7*(4), 1285–1296. https://doi.org/10.5194/cp-7-1285-2011
40. Barker, S., Greaves, M., & Elderfield, H. (2003). A study of cleaning

procedures used for foraminiferal Mg/Ca paleothermometry. *Geochemistry, Geophysics, Geosystems*, *4*(9), n/a-n/a. https://doi.org/10.1029/2003GC000559

41. Rostek, F., Bard, E., Beaufort, L., Sonzogni, C., & Ganssen, G. (1997). Sea surface temperature and productivity records for the last 240 kyr on the Arabian Sea. *Deep-Sea Research Part II: Topical Studies in Oceanography*, *44*(6–7), 1461–1480. https://doi.org/10.1016/S0967-0645(97)00008-8
42. Bassinot, F. C., Beaufort, L., Vincent, E., Labeyrie, L. D., Rostek, F., Müller, P. J., Quidelleur, X., & Lancelot, Y. (1994). Coarse fraction fluctuations in pelagic carbonate sediments from the tropical Indian Ocean: A 1500-kyr record of carbonate dissolution. *Paleoceanography*, *9*(4), 579–600. https://doi.org/10.1029/94PA00860
43. Mohtadi, M., Lückge, A., Steinke, S., Groeneveld, J., Hebbeln, D., & Westphal, N. (2010). Late Pleistocene surface and thermocline conditions of the eastern tropical Indian Ocean. *Quaternary Science Reviews*, *29*(7), 887–896. https://doi.org/https://doi.org/10.1016/j.quascirev.2009.12.006
44. Xu, J., Holbourn, A., Kuhnt, W., Jian, Z., & Kawamura, H. (2008). Changes in the thermocline structure of the Indonesian outflow during Terminations I and II. *Earth and Planetary Science Letters*, *273*(1–2), 152–162. https://doi.org/10.1016/j.epsl.2008.06.029
45. Zuraida, R., Holbourn, A., Nürnberg, D., Kuhnt, W., Dürkop, A., & Erichsen, A. (2009). Evidence for Indonesian Throughflow slowdown during Heinrich events 3 to 5. *Paleoceanography*, *24*(2), n/a-n/a. https://doi.org/10.1029/2008PA001653
46. Herbert, T. D., Peterson, L. C., Lawrence, K. T., & Liu, Z. (2010). Tropical ocean temperatures over the past 3.5 million years. *Science*, *328*(5985), 1530–1534. https://doi.org/10.1126/science.1185435
47. De Garidel-Thoron, T., Rosenthal, Y., Bassinot, F., & Beaufort, L. (2005). Stable sea surface temperatures in the western Pacific warm pool over the past 1.75 million years. *Nature*, *433*(7023), 294–298. https://doi.org/10.1038/nature03189
48. Lisiecki, L. E., & Raymo, M. E. (2005). A Pliocene-Pleistocene stack of 57

globally distributed benthic δ 18O records. *Paleoceanography*. https://doi.org/10.1029/2004PA001071

49. de Boer, B., Lourens, L. J., & Van De Wal, R. S. W. (2014). Persistent 400,000-year variability of Antarctic ice volume and the carbon cycle is revealed throughout the Plio-Pleistocene. *Nature Communications*, *5*. https://doi.org/10.1038/ncomms3999
50. Braconnot, P., Harrison, S. P., Kageyama, M., Bartlein, P. J., Masson-Delmotte, V., Abe-Ouchi, A., Otto-Bliesner, B., & Zhao, Y. (2012). Evaluation of climate models using palaeoclimatic data. *Nature Climate Change 2012 2:6*, *2*(6), 417–424. https://doi.org/10.1038/nclimate1456
51. Howell, P., Pisias, N., J.Ballance, J. Baughman, and L. Ochs, 2006. ARAND. https://github.com/jesstierney/arand.
52. van der Lubbe, H. J. L., Hall, I. R., Barker, S., Hemming, S. R., Baars, T. F., Starr, A., Just, J., Backeberg, B. C., & Joordens, J. C. A. (2021). Indo-Pacific Walker circulation drove Pleistocene African aridification. Nature 598, 618-623. https://doi.org/10.1038/s41586-021-03896-3
53. Ahn, S., Khider, D., Lisiecki, L. E., & Lawrence, C. E. (2017). A probabilistic Pliocene–Pleistocene stack of benthic δ18O using a profile hidden Markov model. *Dynamics and Statistics of the Climate System*, *2*(1). https://doi.org/10.1093/climsys/dzx002
54. Bereiter, B., Eggleston, S., Schmitt, J., Nehrbass-Ahles, C., Stocker, T. F., Fischer, H., Kipfstuhl, S., & Chappellaz, J. (2015). Revision of the EPICA Dome C CO 2 record from 800 to 600 kyr before present. *Geophysical Research Letters*, *42*(2), 542–549. https://doi.org/10.1002/2014GL061957
55. Bouvier-Soumagnac, Y., & Duplessy, J.-C. (1985). Carbon and oxygen isotopic composition of planktonic foraminifera from laboratory culture, plankton tows and Recent sediment; implications for the reconstruction of paleoclimatic conditions and of the global carbon cycle. *Journal of Foraminiferal Research*, *15*(4), 302–320. http://dx.doi.org/10.2113/gsjfr.15.4.302
56. Pearson, P. N. (2012). Oxygen Isotopes in Foraminifera: Overview and Historical Review. *The Paleontological Society Papers*, *18*, 1–38.

https://doi.org/10.1017/s1089332600002539

57. Spratt, R. M., & Lisiecki, L. E. (2016). A Late Pleistocene sea level stack. *Climate of the Past*, *12*(4), 1079–1092. https://doi.org/10.5194/cp-12-1079-2016
58. Laskar, J., Robutel, P., Joutel, F., Gastineau, M., Correia, A. C. M., & Levrard, B. (2004). A long-term numerical solution for the insolation quantities of the Earth. *Astronomy & Astrophysics*, *428*(1), 261–285. https://doi.org/10.1051/0004-6361:20041335
59. Johnson, T. C., Werne, J. P., Brown, E. T., Abbott, A., Berke, M., Steinman, B. A., Halbur, J., Contreras, S., Grosshuesch, S., Deino, A., Scholz, C. A., Lyons, R. P., Schouten, S., & Damsté, J. S. S. (2016). A progressively wetter climate in southern East Africa over the past 1.3 million years. *Nature*, *537*(7619), 220–224. https://doi.org/10.1038/nature19065
60. Kathayat, G., Cheng, H., Sinha, A., Spötl, C., Edwards, R. L., Zhang, H., Li, X., Yi, L., Ning, Y., Cai, Y., Lui, W. L., & Breitenbach, S. F. M. (2016). Indian monsoon variability on millennial-orbital timescales. *Scientific Reports*, *6*(1), 24374. https://doi.org/10.1038/srep24374
61. Cheng, H., Edwards, R. L., Sinha, A., Spötl, C., Yi, L., Chen, S., Kelly, M., Kathayat, G., Wang, X., Li, X., Kong, X., Wang, Y., Ning, Y., & Zhang, H. (2016). The Asian monsoon over the past 640,000 years and ice age terminations. *Nature*, *534*(7609), 640–646. https://doi.org/10.1038/nature18591
62. de Boer, B., van de Wal, R. S. W., Lourens, L. J., Bintanja, R., & Reerink, T. J. (2013). A continuous simulation of global ice volume over the past 1 million years with 3-D ice-sheet models. *Climate Dynamics*, *41*(5), 1365–1384. https://doi.org/10.1007/s00382-012-1562-2
63. Elderfield, H., Ferretti, P., Greaves, M., Crowhurst, S., McCave, I. N., Hodell, D., & Piotrowski, A. M. (2012). Evolution of ocean temperature and ice volume through the mid-Pleistocene climate transition. *Science*, *337*(6095), 704–709. https://doi.org/10.1126/SCIENCE.1221294/
64. Shackleton, N. J. (1987). Oxygen isotopes, ice volume and sea level. *Quaternary Science Reviews*, *6*(3–4), 183–190. https://doi.org/10.1016/0277-3791(87)90003-5

65. Grant, K. M., Rohling, E. J., Bronk Ramsey, C., Cheng, H., Edwards, R. L., Florindo, F., Heslop, D., Marra, F., Roberts, A. P., Tamisiea, M. E., & Williams, F. (2014). Sea-level variability over five glacial cycles. *Nature Communications 2014 5:1*, *5*(1), 1–9. https://doi.org/10.1038/ncomms6076
66. Wang, P., Tian, J., & Lourens, L. J. (2010). Obscuring of long eccentricity cyclicity in Pleistocene oceanic carbon isotope records. *Earth and Planetary Science Letters*, *290*(3–4), 319–330.
67. U.K. Met Office (2010). Cartopy: A cartographic python library with a matplotlib interface. *Exeter, Devon*.
68. Natural Earth (2015). Free vector and raster map data. Available at www.naturalearthdata.com

ACKNOWLEDGEMENTS

The authors would like to thank the members and crew of IODP expedition 361 for their work in collecting and providing the samples. We further extend our thanks to Pippa Whitehouse and three anonymous reviewers for supporting and improving the manuscript. This work was mainly funded through UK NERC grant NE/P000878/1 provided by S.B. J.W.B.R. received funding for this work from the European Research Council under the European Union's Horizon 2020 research and innovation program (grant agreement 805246) which also funded M.D.D. S.N received further funds from the Ministry of Science and Technology, Taiwan (MOST 111-2636-M-002-020) granted to Haojia Ren. X.Z, and Y.S. were funded through the Natural Science Foundation of China (41988101, 42075047) and German Helmholtz Postdoc Program (PD-301). H.T.M was funded through the Ministry of Science and Technology, Taiwan (110-2811-M-002-647, 111-2811-M-002-116).

AUTHOR CONTRIBUTIONS

S.N. collected, analysed and interpreted the data. S.N. wrote the paper, with support from all co-authors. J.W.B.R., M.B.A., and S.B. supported the collection, analysis, and interpretation of the data, and provided the grant. X.Z. and Y.S. conducted the GCM model simulations and supported the interpretation of the results. M.D.D. computed the data stacks and supported the interpretation of the results. B.dB. and H.T.M. conducted model runs and postprocessing of sea level and land/sea ratio reconstructions and supported the interpretation of the results. The samples were collected by S.B. and I.R.H on IODP expedition 361. All authors provided comments on the final manuscript.

AUTHOR INFORMATION

Competing interests

The authors declare no competing interests.

Corresponding author

Correspondence to Sophie Nuber (snuber@ntu.edu.tw)

EXTENDED DATA LEGENDS

Extended Data Fig. 1 U1476 sea surface hydrography reconstructions in comparison to U1476 benthic oxygen isotopes

(a), (c), and (f) benthic foraminifera $\delta^{18}O$[51] on inverted y-axes (light blue lines), (b) planktonic $\delta^{18}O_{carbonate}$ from *G. ruber* on inverted y-axis (green line; this study), (d) planktonic Mg/Ca with log-scale y-axis and (e) calculated SSTs (red line; this study) with Monte-Carlo propagated errors including analysis, age model, and equation calibration errors plotted as red shaded envelope, (g) calculated ice-volume corrected $\delta^{18}O_{sw\text{-}ivc}$ for the surface ocean as proxy for salinity, derived from the $\delta^{18}O_{G.\ ruber}$ and SST records (dark green; this study) with propagated errors including Monte-Carlo SST-, and $\delta^{18}O_{G.\ ruber}$ -analysis errors plotted as dark green shaded envelope. The centre of each deglaciation is indicated by dashed vertical lines and labelled T1 to T16. Note the increases in SST and $\delta^{18}O_{sw\text{-}ivc}$ during glacial periods (grey shaded bars).

Extended Data Fig. 2 Derivation and alternative derivations of the newly presented climate proxies

(a) Atmospheric CO_2 from Antarctic ice cores[53] (pink) and calculated using linear transfer from the LR04 benthic $\delta^{18}O$ stack[48] (dark red), which is plotted in (b). (c) Resulting SST calculations using the method of ref.[9] with ice core CO_2[53] (pink), and LR04[48]-based CO_2 (dark red). (d) Difference between $\delta^{18}O$ of global ice volume[49] (blue) and U1476 seawater (this study) prior to the ice volume correction (green). The large difference suggests that there is a substantial local salinity signal which cannot be explained by whole ocean changes. (e) Age model comparison using benthic $\delta^{18}O$ for all sites in Fig. 2 (this study and refs[23,28,29]). (f) U1476 salinity proxy (dark green; this study); dark green diamonds highlight times of salinification onset, and (g) GMSL[49] (pink) highlighting sea level stands at times of salinification onset in pink dots. The analysis corresponds to Fig. 2e, f, and results in the same average GMSL stand (dashed pink line) at which salinification occurs. Deglaciations are plotted as dashed vertical lines, and intervals of rising $\delta^{18}O_{sw\text{-}ivc}$ prior to each glacial termination are indicated with vertical grey bars. Note y-axes in (b), (d), and (e) are inverted.

Extended Data Fig. 3 Indian Ocean salinity and temperature stack construction

(a) Age model comparison using benthic $\delta^{18}O$ for all cores included in the stacks on an inverted y-axis. The colours of the labels correspond to the coloured lines in all panels. References for all cores are listed in Figure 1 and Methods. (b) All SST records which are included in the SST stack. (c) All salinity proxy records which are included in the salinity stack. (d) z-scores of all SST records included in the SST stack, the SST stack (thick black line) with 95^{th} percentile error envelope (grey shaded band), and an SST stack excluding U1476 data with 95^{th} percentile envelope (orange shaded band). (e) z-scores of all salinity proxy records included in the salinity stack, the salinity stack (thick black line) with 95^{th} percentile error envelope (grey shaded band), and a salinity stack excluding U1476 data with 95^{th} percentile envelope (orange shaded band). Note that there is no difference in the onset of the salinification and warming between the black and orange stacks suggesting that U1476 does not force the stack calculations. Intervals of rising $\delta^{18}O_{sw-ivc}$ prior to each glacial termination are indicated with vertical grey bars.

Extended Data Fig. 4 Salinity reconstruction using different global mean sea level corrections

(a) $\delta^{18}O_{sw-ivc}$ records derived using 4 different GMSL reconstructions for the ice volume correction. U1476 $\delta^{18}O_{benthic}$[51] is plotted in b) for lead-lag comparison. Grey bars highlight the early increase in $\delta^{18}O_{sw-ivc}$ prior to terminations. The ref.[49] ice volume correction allowed modelled ice volume $\delta^{18}O$ to be used (dark green). For other GMSL reconstructions[64,65], a change of 1 % in $\delta^{18}O_{benthic}$ per 120 m GMSL, or maximum reconstructed GMSL was assumed. The colour of each $\delta^{18}O_{sw-ivc}$ record corresponds with the referenced scenario in the other panels. (c) Absolute $\delta^{18}O_{sw-ivc}$ amplitude of the glacial $\delta^{18}O_{sw-ivc}$ maxima compared to the preceding minima for all 4 $\delta^{18}O_{sw-ivc}$ scenarios. The colours of the bars correspond to the referenced scenarios in (a). Note that differences between different scenarios are relatively small. (d) Corresponding ice volume $\delta^{18}O$ curves for the 4 GMSL reconstructions. The colours of each line correspond with the referenced scenario in (a). Intervals of rising $\delta^{18}O_{sw-ivc}$ prior to each glacial termination are indicated with vertical grey bars in (a). Note y-axes in (b) and (d) are inverted.

Extended Data Fig. 5 Surface hydrography in the source regions of the ITF and Indian Ocean

(a) U1476 $\delta^{18}O_{sw-ivc}$ (dark green), (b) U1476 Mg/Ca-derived sea surface temperatures (orange) (this study), and (c) U1476 $\delta^{18}O_{benthic}$[51] (thin blue line) from the western Indian Ocean. (d) Alkenone-derived sea surface temperatures (light pink) and (e) $\delta^{18}O_{benthic}$ (thin blue line) from the South China Sea[46]. (f) Mg/Ca-derived sea surface temperatures (brown) and (g) $\delta^{18}O_{benthic}$ (thin blue line) from the western Pacific warm pool[47]. Onset of U1476 glacial salinification highlighted in grey bars. Note that both

South China Sea, and western Pacific warm pool records do not show a similarly consistent lead-lag pattern between their respective SST and $\delta^{18}O_{benthic}$ data. Note $\delta^{18}O_{benthic}$ data is presented on inverted y-axes.

Extended Data Fig. 6 Spectral analysis results for U1476 climate proxies

Spectral analysis of U1476 SST (a), $\delta^{18}O_{sw-ivc}$ (b), and $\delta^{18}O_{benthic}$[51] (c); as well as SST z-score stack (e), $\delta^{18}O_{sw-ivc}$ z-score stack (f), and LR04 $\delta^{18}O_{benthic}$ stack for comparison (g). Peaks above the red line are significant at the 95% interval. Black dashed vertical lines indicate precession (23 kyr), obliquity (41 kyr), and eccentricity (100 kyr) periodicities.

Extended Data Fig. 7 Cross spectral analysis results for U1476 climate proxies showing lead-lag characteristics

Cross spectral analyses showing coherence (red) and phase (black) between U1476 SST, $\delta^{18}O_{sw-ivc}$, and $\delta^{18}O_{benthic}$[51] (top, a-c); and SST stack, $\delta^{18}O_{sw-ivc}$ stack, and LR04 $\delta^{18}O_{benthic}$ stack[48] (bottom, d-f). Coherence data above the red, and purple, line indicates significant coherence between datasets at the 95 %, and 80 %, significance level. Phase data at times of significant coherence above the black line (Phase = 0) indicate significant lead of the first variable. Precession (23 kyr), obliquity (41 kyr), and eccentricity (100 kyr) periodicities are indicated by vertical black dashed lines.

Extended Data Fig. 8 Spectral and cross-spectral analysis results for previously published hydrography data from U1446 in the Bay of Bengal

(a) Spectral analysis of $\delta^{18}O_{benthic}$, and (b) $\delta^{18}O_{sw-ivc}$. (c) Phase and coherence between $\delta^{18}O_{benthic}$ and $\delta^{18}O_{sw-ivc}$. Black horizontal line shows Phase = 0; positive/negative phase values indicate 1st variable/2nd variable in the header leading the other variable. Vertical brown line indicates coherence 95% confidence interval. Precession (23kyr), obliquity (41kyr), and eccentricity (100kyr) periodicities are indicated by vertical black dashed lines. All data that went into this analysis was previously published in (ref)[14].

Extended Data Fig. 9 Indian Ocean hydroclimate proxies compared to U1476 salinity

(a) 15° S July summer insolation[57]. (b) – (d), (f), (h), (j), (l), (n), (p) U1476 $\delta^{18}O_{sw\text{-}ivc}$ (this study). (c) U1476 $\delta^{18}O_{benthic}$[51] on inverted y-axis. (e) Malawi Lake SST, proxy for African Monsoon variability[58]. (g) Speleothem $\delta^{18}O_{CaCO_3}$ from Dongge Cave, China, proxy for Southeast Asian Summer Monsoon variability[60]. (i) Speleothem $\delta^{18}O_{CaCO_3}$ from Bittoo Cave, India, proxy for Indian Summer Monsoon variability[59]. (k) TY93-929/P $\delta^{18}O_{sw\text{-}ivc}$, Arabian Sea surface ocean salinity proxy[40]. (m) U1446 $\delta^{18}O_{sw\text{-}ivc}$, Bay of Bengal sea surface salinity proxy[14]. (o) GeoB10038-4 $\delta^{18}O_{sw\text{-}ivc}$[43], eastern Indian Ocean. Grey vertical bars highlight the period of salinification in U1476 which is also visible in the Arabian Sea, Bay of Bengal, and eastern Indian Ocean sea surface salinity proxies.

Extended Data Fig. 10 Changes in land surface as a function of changes in global mean sea level

(a) Pixels occurring within the orange polygon were used to calculate the land/sea ratio in each time-slice map created by the ANICE-SELEN model. (b) Change in land to sea surface ratio in the Indonesian archipelago as modelled by the coupled ice sheet-topography model ANICE-SELEN for a subset of 9 glacial-interglacial cycles in respect to GMSL. Changes occurring from falling and rising sea level are plotted in blue and orange respectively – the hysteresis between falling and rising sea levels results from the delayed response of the solid Earth to changes in ocean water surface loading. (c) Slope of the land/sea surface ratio as a function of GMSL to highlight specific sea levels at which the rate of land exposure during sea level fall, or land flooding during sea level rise, is particularly fast with respect to the change in GMSL. Vertical blue shaded bars highlight the GMSL interval within which the change in ratios at GMSL fall is particularly fast. The map in (a) was plotted using the library Cartopy[66] in Python. Outlines for countries are taken from ref[67].

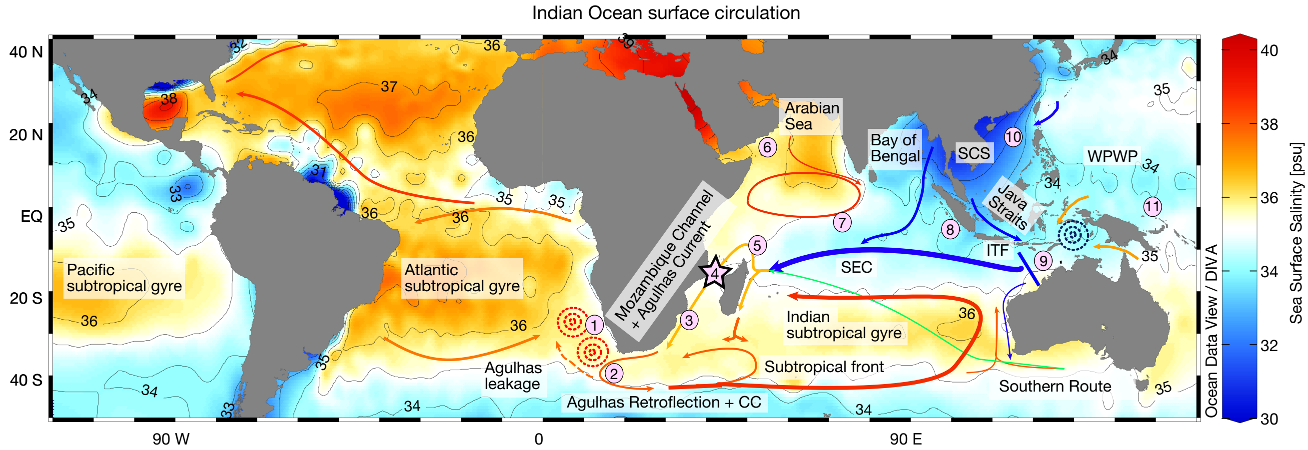
Indian Ocean surface circulation
40 N
20 N
EQ
20 S
40 S
90 W
0
90 E
Pacific
subtropical gyre
Atlantic
subtropical gyre
Agulhas
leakage
Agulhas Retroflection + CC
Mozambique Channel
+ Agulhas Current
Arabian
Sea
Bay of
Bengal
SCS
WPWP
Java
Straits
ITF
SEC
Indian
subtropical gyre
Subtropical front
Southern Route
Ocean Data View / DIVA
Sea Surface Salinity [psu]
40
38
36
34
32
30

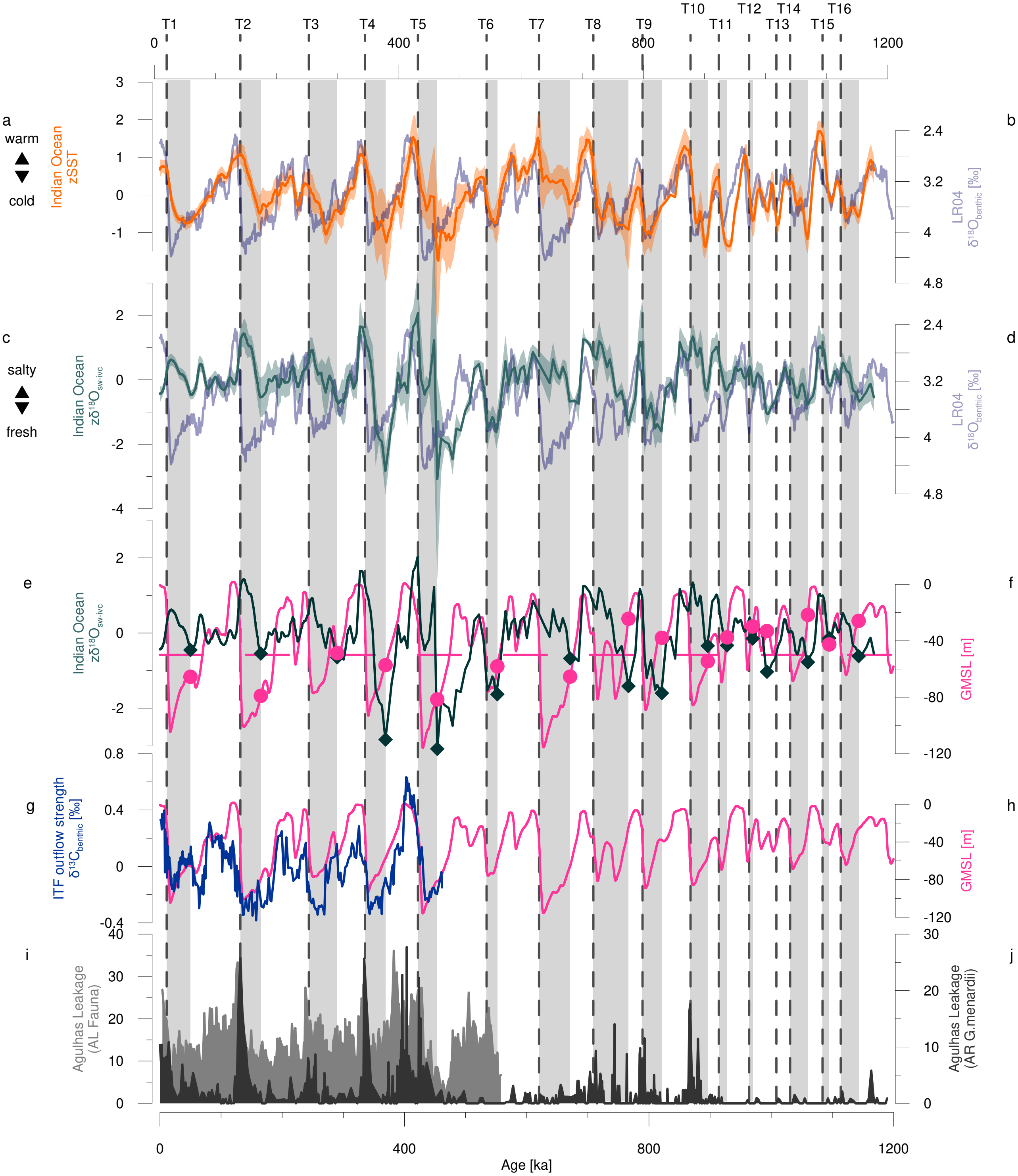

T1
T2
T3
T4
T5
T6
T7
T8
T9
T10
T11
T12
T13
T14
T15
T16
a
warm
cold
Indian Ocean
zSST
b
LR04
δ18Obenthic [‰]
c
salty
fresh
Indian Ocean
zδ18Osw-ivc
d
e
f
GMSL [m]
g
ITF outflow strength
δ13Cbenthic [‰]
h
i
Agulhas Leakage
(AL Fauna)
j
Agulhas Leakage
(AR G.menardii)
Age [ka]

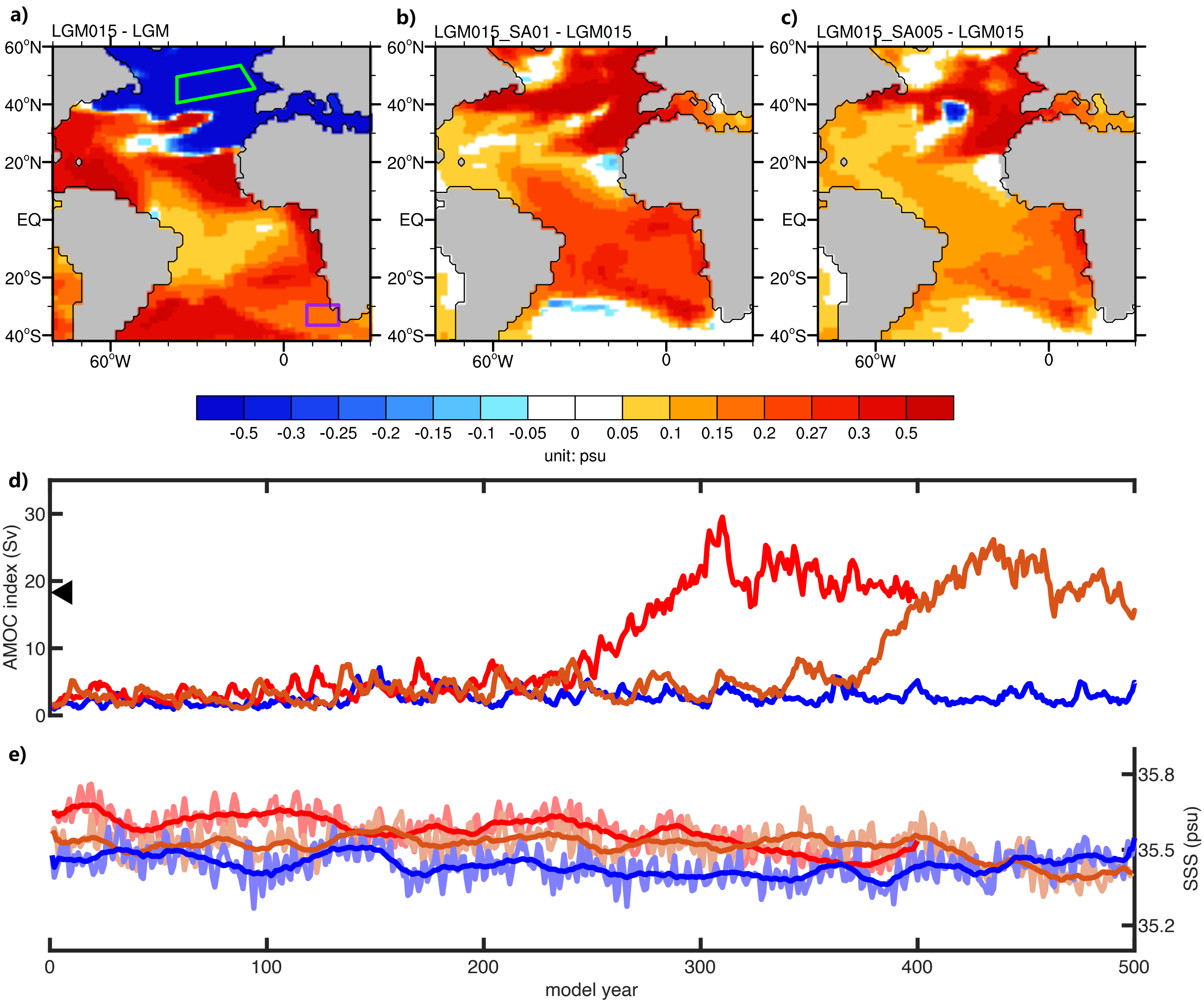

a)
LGM015 - LGM
b)
LGM015_SA01 - LGM015
c)
LGM015_SA005 - LGM015
60°N
40°N
20°N
EQ
20°S
40°S
60°W
0
-0.5
-0.3
-0.25
-0.2
-0.15
-0.1
-0.05
0
0.05
0.1
0.15
0.2
0.27
0.3
0.5
unit: psu
d)
AMOC index (Sv)
30
20
10
0
e)
SSS (psu)
35.8
35.5
35.2
0
100
200
300
400
500
model year

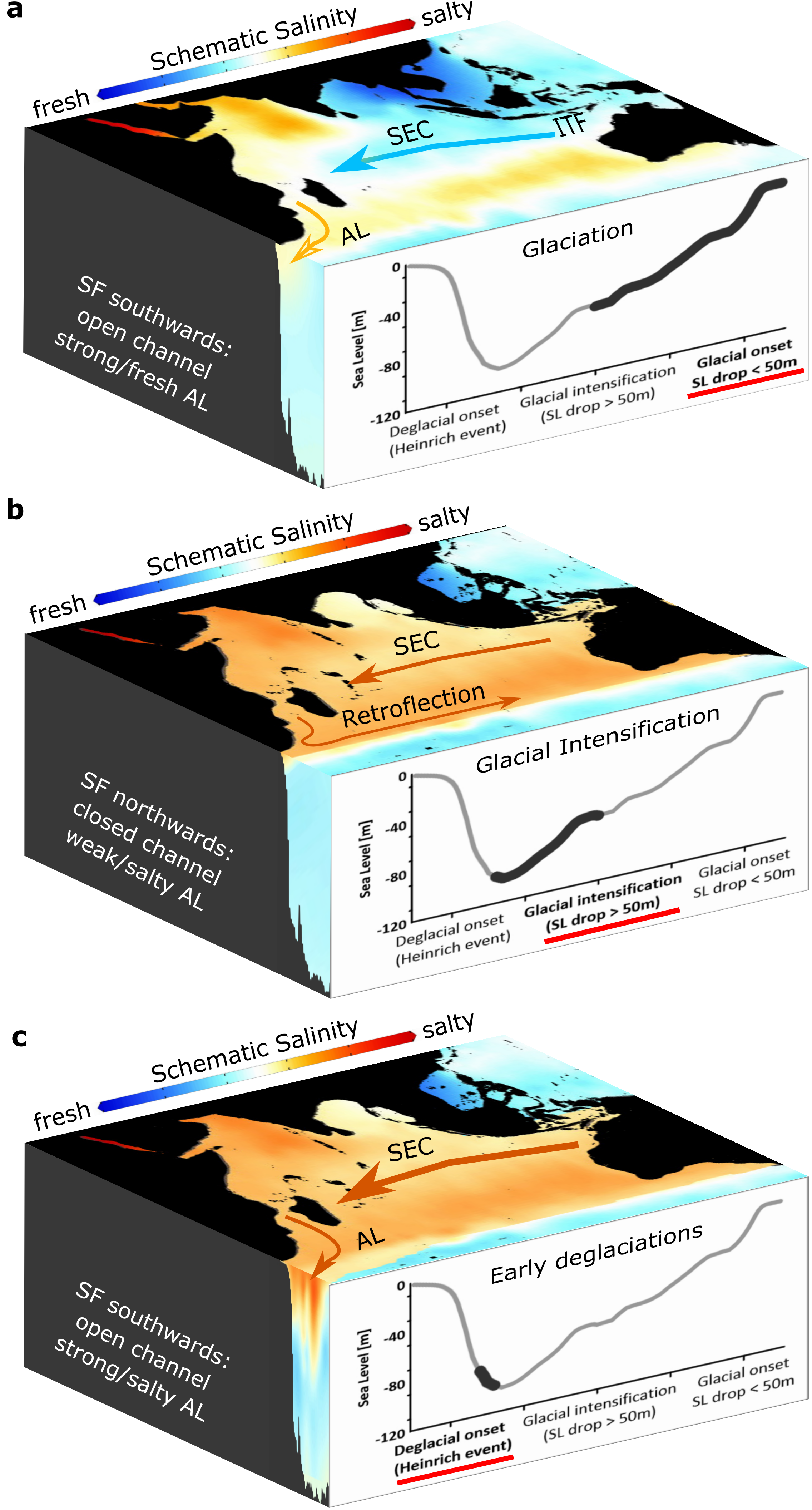

a
fresh
Schematic Salinity
salty
SEC
ITF
AL
Glaciation
SF southwards:
open channel
strong/fresh AL
Sea Level [m]
0
-40
-80
-120
Deglacial onset
(Heinrich event)
Glacial intensification
(SL drop > 50m)
Glacial onset
SL drop < 50m
b
fresh
Schematic Salinity
salty
SEC
Retroflection
Glacial Intensification
SF northwards:
closed channel
weak/salty AL
Sea Level [m]
0
-40
-80
-120
Deglacial onset
(Heinrich event)
Glacial intensification
(SL drop > 50m)
Glacial onset
SL drop < 50m
c
fresh
Schematic Salinity
salty
SEC
AL
Early deglaciations
SF southwards:
open channel
strong/salty AL
Sea Level [m]
0
-40
-80
-120
Deglacial onset
(Heinrich event)
Glacial intensification
(SL drop > 50m)
Glacial onset
SL drop < 50m